

Investigation of Circulation Flow and Slag-Metal Behavior in an Industrial Single Snorkel Refining Furnace (SSRF): Application to Desulfurization



WEIXING DAI, GUOGUANG CHENG, GUOLEI ZHANG, ZHIDONG HUO, PEIXIAN LV, YUNLONG QIU, and WEIFEI ZHU

A combined method of mathematical and physical modeling was used to investigate the circulation flow and slag-metal behavior in industrial SSRF and RH. The circulation flow of molten steel was simulated by using the coupled mathematical model. The results indicate that two different circulation modes are presented separately in SSRF and RH. The incomplete exchange of molten steel was found in SSRF because of the interaction between upflow and downflow in the snorkel, while the molten steel is fully exchanged between the vacuum chamber and ladle in RH. The flow behavior of top slag in the vacuum chamber was further investigated and compared by using cold models. It was found that many slag droplets are generated in the vacuum chamber, and then dragged into ladle by downflow for both reactors. The main difference is that the majority of droplets eventually float into ladle slag in RH, while most of the slag droplets in SSRF is cycled repeatedly, which allows slag droplets to have a longer time to contact with steel. Thus, the slag-steel reaction is more adequate in SSRF. Furthermore, the industrial desulfurization tests were designed to verify the difference in the refining effect between the two kinds of droplet behavior in actual production. The results indicate that the higher desulfurization degree was realized in SSRF with less consumption of argon than that of RH.

<https://doi.org/10.1007/s11663-020-01781-4>

© The Minerals, Metals & Materials Society and ASM International 2020

I. INTRODUCTION

IN the 1970s, the Single Snorkel Refining Furnace (SSRF) was originally exploited through the reformation of RH to improve refining efficiency for small capacity ladle in China,^[1] and now it has been developed as a multifunctional vacuum refining equipment for the mass production of special steel.^[2,3] Subsequently, a similar degasser named Revolutionary Degassing Activator (REDA) was independently developed by Nippon Steel Corporation in the 1990s, and now it has been steadily applied to the manufacture of ultra-low carbon steel.^[4-8]

The circulation principle of SSRF can be depicted in Figure 1; the lifting gas is blown from the ladle bottom, and the hot metal is circulated between the ladle and vacuum chamber through a large-size snorkel. Owing to the large injection depth and the reduced pressure, a large bubble-activated surface can be obtained in the vacuum chamber,^[9,10] which allows the molten steel to realize high-efficiency removals of carbon, hydrogen, and nitrogen from the molten steel. It is well known that the reasonable flow field is one of the important prerequisites for efficient refining. Concerning this topic, many cold experiments^[11-13] and mathematical modeling^[14-16] have been performed to investigate the effect of various parameters on the flow field in SSRF or REDA, including gas injecting position, gas flow rate, snorkel diameter, immersion depth, *etc.* Most of these researches focused on the optimization of the flow field of molten steel, while the flow behavior of the slag layer in ladle or vacuum chamber is rarely noticed. In practice, the ladle slag is usually covered above the molten steel, while the top slag in the vacuum chamber is controlled according to the needs of the process. For decarburization and degassing, the operation of slag-discharge is performed before vacuuming to avoid the ladle slag entering the vacuum chamber and thus reducing reaction

WEIXING DAI, GUOGUANG CHENG, and GUOLEI ZHANG are with the State Key Laboratory of Advanced Metallurgy, University of Science and Technology Beijing, Beijing, 100083, P.R. China. Contact e-mail: chengguoguang@metall.ustb.edu.cn ZHIDONG HUO and PEIXIAN LV are with the Zhejiang Hangzhen Energy Technology Co., Ltd, Hangzhou, 311121, P.R. China. YUNLONG QIU and WEIFEI ZHU are with the Zhongxing Energy Equipment Co., Ltd, Nantong, 226126, P.R. China.

Manuscript submitted July 11, 2019.

Article published online February 3, 2020.

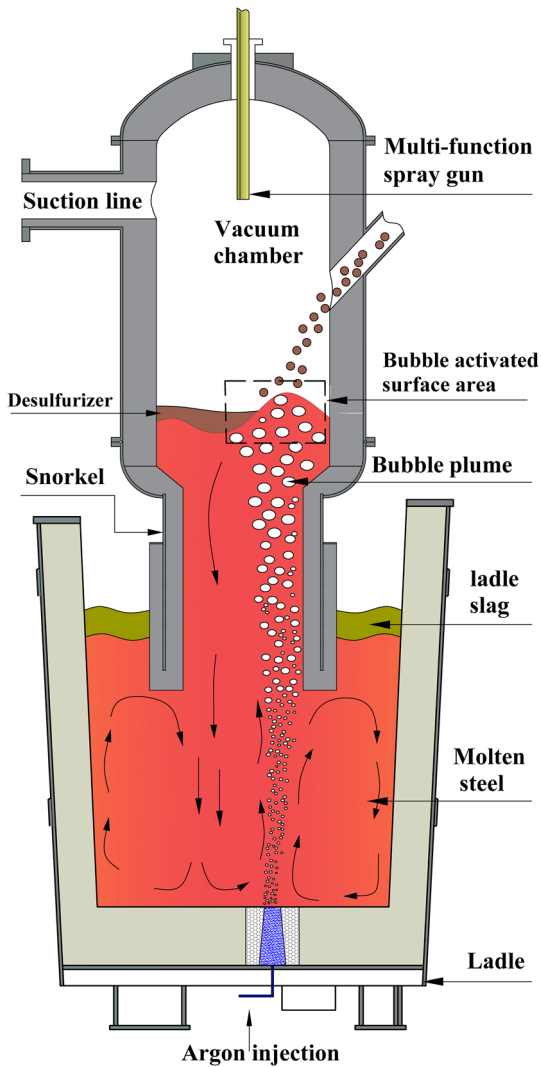


Fig. 1—The sketch diagram of the SSRF.

efficiency.^[17,18] For desulfurization process, the desulfurizer is usually added from the vacuum chamber after slag-discharge. Just as RH reactor is widely applied to produce ultra-low sulfur steel,^[17] the SSRF has the same advantages as RH for deep desulfurization, that is, strong steel circulation, getting rid of the effect of ladle top slag on the composition of desulfurizer, and avoiding absorption nitrogen because of the closed atmosphere.

A lot of researchers have contributed to analyzing kinetic and thermodynamic conditions of RH desulfurization reaction combining with the practical process over the past few decades.^[19–22] Although conflicting viewpoints have been presented on which factor (sulfide capacity, temperature, desulfurizer composition, *etc.*) played the dominant role in vacuum desulfurization reaction, a basic agreement has been reached, that is increasing contact area and resident time between desulfurizer and liquid steel can effectively improve desulfurization efficiency. To increase the contact area, various desulfurization techniques have been developed in the RH process, such as RH-OP,

RH-PB, RH-PTB. The powdery desulfurizer is directly injected into the liquid steel to increase the contact area. Peixoto *et al.*^[23] investigated the movement, distribution, and size of slag droplets in RH system; the results indicate that liquid slag layer is dispersed into fine droplets due to the strong turbulence inside the vacuum chamber, these droplets are dragged into the ladle through the down-leg by rapid steel circulation, and the residence time of droplets in liquid steel can be delayed by properly reducing the gas flow rate. Owing to the different furnace structure and blowing method between SSRF and RH, the circulation flow of liquid steel in the snorkel and vacuum chamber presents a large difference. Thus, there are reasons to believe that the flow pattern of slag droplets in SSRF could be different from RH. However, there are very few studies covering this topic due to the limited industrial application of SSRF in desulfurization. Qin *et al.*^[24] and Rui *et al.*^[25] have reported the comparative desulfurization effect between SSRF and RH; the results shown that a higher desulfurization degree was achieved in SSRF with the lower consumption of desulfurizer and argon. But the reason for this improvement was not clarified. Therefore, a more detailed analysis of the desulfurization should be concerned with SSRF.

In the present study, an industrial 80t-SSRF was selected as the research object, which was built through the modification of the original 80t-RH. The objective of this work is to investigate the circulation flow of liquid steel and flow behavior of top slag in the vacuum chamber, and provide some additional information to understand desulfurization process in SSRF better. Meanwhile, the circulation flow of the original RH also was investigated to make a comparison with the current SSRF. A method of combining numerical simulation with the cold model was used to carry out this objective. Besides that, the industrial tests were conducted to compare the desulfurization degree between RH and SSRF.

II. METHODOLOGY

A. Cold Modeling

Depending on geometric and dynamic similarity criteria, two cold models (RH and SSRF) were fabricated with a scale ratio ($\lambda = 0.3 : 1$). Table I shows the main structure parameters and operating conditions of the model and the industrial reactor. The layout of the industrial nozzle is shown in Figure 2, and a porous brick is implemented in SSRF, positioned at the ladle bottom on the half radius of the snorkel. Eight nozzles are arranged at the height of 25cm above the bottom of the up-snorkel in RH. The gas flow rate of the model was calculated by Eq. [1] based on the dynamic similarity of fluid in the reactor,^[26]

$$Q_m = 0.817 \cdot \lambda^{2.5} Q_p, \quad [1]$$

where Q_m is gas flow rate in the cold model, Q_p is gas flow rate in the actual reactor.

Table I. Geometry Parameters of the Actual Reactors and Cold Models

Parameters	Prototype		Scaled Water Model	
	SSRF	RH	SSRF	RH
Diameter of Snorkel, m	1.0	0.45	0.30	0.135
Diameter of Vacuum Chamber, m	1.3	1.3	0.39	0.39
Length of Snorkel, m	1.50	1.50	0.45	0.45
Vacuum Pressure, Pa	1333	1333	97000	97000
Snorkel Immersion Depth, m	0.4	0.4	0.12	0.12
Nozzle Number/Diameter, mm	1/120	8/8	1/36	8/2.4
Argon Flow Rate, NL/min	100–500	600–1500	4–20	24–60
Nozzle Height Above Snorkel Bottom, m	—	0.23	—	0.07
Up/Down Diameter of Ladle, m	2.6/2.2	—	0.78/0.66	—
Height of Ladle, m	3.11	—	0.933	—
Initial Steel Depth in Ladle, m	2.6	—	0.78	—
Initial Slag Thickness in the Ladle, mm	100	—	—	—

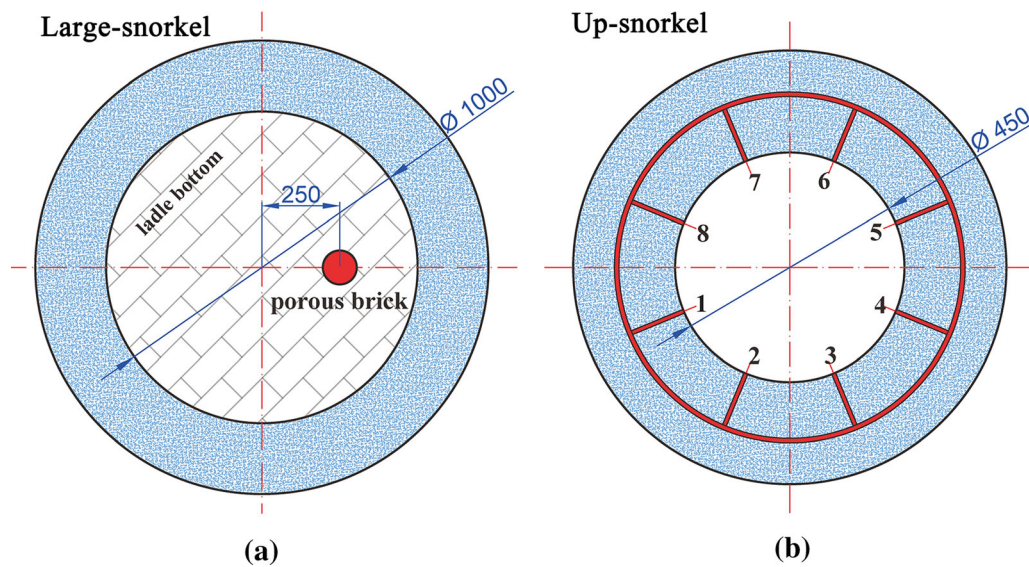


Fig. 2—The arrangement of the gas nozzle in industrial reactors: (a) SSRF, (b) RH.

For a better understanding of the cold setup, a schematic view of the arrangement is depicted in Figure 3. A vacuum pump was connected to the vacuum chamber, and the pressure was controlled manually using a system of valves and monitored by a vacuumeter. Water and compressed air were used to represent liquid steel and argon, and *N*-pentane was selected as top slag in the vacuum chamber because the density ratio of the *N*-pentane/water system is very close to slag/steel system.^[23,27] The *N*-pentane oil is a colorless transparent liquid and insoluble in water. For better visualization, the *N*-pentane was colored by a kind of blue oil-soluble liquid dye, which is easily soluble in *N*-pentane but insoluble in water. The volume ratio of dye/*N*-pentane was controlled at 1/100. The material properties of these fluids are listed in Table II. A high-speed video camera was employed to capture the

motion of the slag droplets in the vacuum chamber and ladle. Moreover, the mixing experiments were performed to verify the reliability of the mathematical model, and the mixing time was measured *via* a conductivity technique.^[28–30] The saturated KCl solution was poured into the vacuum chamber, and then its concentration was detected simultaneously by a conductivity sensor.

B. Mathematical Modeling

In the present work, the transient flow in reactors was simulated based on the developed model concerning multiphase flow and tracer transport behavior in the previous works.^[31] The continuous phases were defined as Newtonian, viscous, and incompressible. The coupled

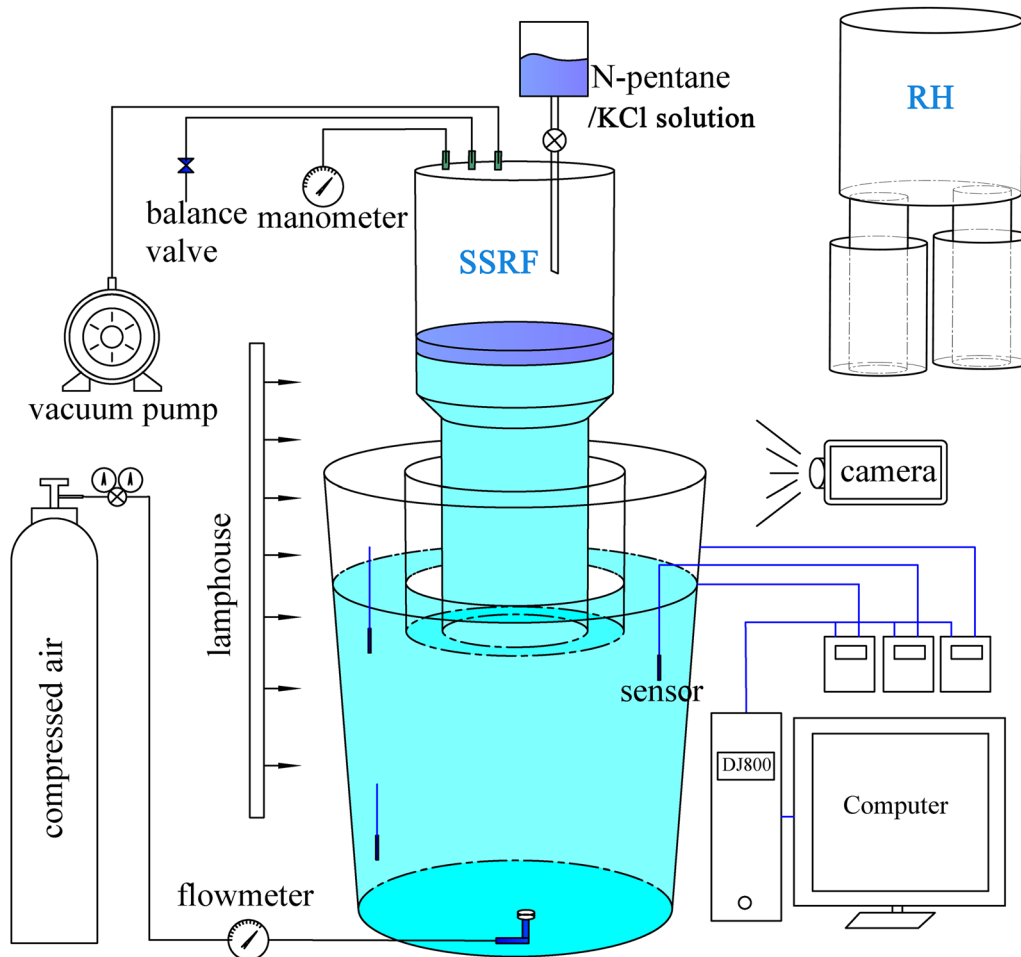


Fig. 3—Schematic diagram of the cold model setup.

Table II. Material Properties of Fluid in the Present Model

Fluid	Density, kg/m ³	Dynamic Viscosity, Pa·s	Interfacial Tension, N/m
Molten Steel	7020	0.0055	1.82, steel/air
Slag	3500	0.05	1.15, steel/slag
Argon	1.623	2.13×10^{-5}	1.89, steel/argon
Air	1.29	8.9×10^{-5}	0.018, <i>N</i> -pentane/air
Water	998.2	8.5×10^{-4}	0.072, air/water
<i>N</i> -Pentane	626	2.3×10^{-4}	0.0057, <i>N</i> -pentane/ water

model VOF (volume of fraction)-DPM (discrete phase model) was used for tracking the free surfaces of continuous phases and tracking trajectories of the discrete argon bubbles, respectively.

1. VOF model

Three continuous phases, *i.e.*, molten steel, slag, and the air above the liquid, were mathematically described by the VOF method based on the Eulerian frame, and it places a strong emphasis on accurate tracking of the interfaces between continuous phases that might be present in the domain. The conservation equations of mass and momentum are written as follows^[32,33]:

$$\frac{1}{\rho_i} \left[\frac{\partial}{\partial t} (\alpha_i \rho_i) + \nabla \cdot (\alpha_i \rho_i u) \right] = 0 \quad [2]$$

$$\frac{\partial}{\partial t} (\rho u) + \nabla \cdot (\rho u) = -\nabla P + \nabla \cdot [\mu (\nabla u + \nabla u^T)] + \rho g + F_b + f_a, \quad [3]$$

where ρ_i and α_i are the density and volume fraction of continuous phase ($\sum_{i=1}^3 \alpha_i = 1$), and u is the mixture

velocity. The surface tension force term (f_s) was considered by applying the continuous surface force (CSF) model.^[34,35] The momentum contribution from bubbles is given as input term to the external force F_b , which can be obtained by summing the forces that are acting on all the bubbles in the cell by the fluid. ρ represents mixture density, which is solved according to the following constraint,

$$\sum_{i=1}^3 \alpha_i \rho_i = \rho. \quad [4]$$

Turbulence in the Eulerian mixture was simulated by the standard $k-\varepsilon$ model.^[36] The equations for the turbulence kinetic energy (k) and the turbulent dissipation rate (ε) are written as

$$\frac{\partial}{\partial t}(k\rho) + \nabla \cdot (\rho k u_i) = \nabla \cdot \left[\left(\mu + \frac{\mu_t}{\sigma_k} \right) \nabla k \right] + G_k - \rho \varepsilon \quad [5]$$

$$\begin{aligned} \frac{\partial}{\partial t}(\varepsilon\rho) + \nabla \cdot (\rho \varepsilon u_i) = \nabla \cdot \left[\left(\mu + \frac{\mu_t}{\sigma_\varepsilon} \right) \nabla \varepsilon \right] \\ + \frac{\varepsilon}{k} (C_{1\varepsilon} G_k - C_{2\varepsilon} \rho \varepsilon) \end{aligned} \quad [6]$$

$$\mu_t = \rho C_\mu k^2 / \varepsilon, \quad [7]$$

where μ_t is the turbulent viscosity, G_k represents the generation of turbulence kinetic energy due to the mean velocity gradients. $C_{1\varepsilon}$, $C_{2\varepsilon}$, C_μ , σ_k , and σ_ε are the empirical constants with values of 1.44, 1.92, 0.09, 1.0, and 1.3, respectively.

2. DPM model

The dispersed argon bubbles were treated as the discrete second phase in the fluid domain. In the Lagrangian framework of the DPM, the trajectory of an individual bubble was calculated by integrating a force balance over it in time and space according to Newton's 2nd Law, which can be described as below equation^[37]:

$$\begin{aligned} \frac{du_b}{dt} = \frac{(\rho_b - \rho)}{\rho_b} \cdot g + C_{VM} \frac{\rho}{\rho_b} \frac{d}{dt}(u - u_b) + \frac{\rho}{\rho_b} u_b \cdot u \\ + F_D(u - u_b). \end{aligned} \quad [8]$$

The four terms on the right are the contributions of gravity and buoyancy force ($F_{G,i} + F_{B,i}$), virtual mass force ($F_{VM,i}$), pressure gradient force ($F_{P,i}$), and drag force ($F_{D,i}$) to bubble acceleration. C_{VM} is the virtual mass factor with a default value of 0.5.^[38]

The drag force is viscous resistance of the steel acting on the bubbles and can be expressed as follows:

$$F_D = \frac{3\mu_m C_D Re_b}{4\rho_b d_b^2} (u_m - u_b), \quad [9]$$

where ρ_b is the density of the bubble, d_b is the diameter of the bubble, Re_b is a function of the relative Rey-

nolds number, and C_D is the drag coefficient. Since the shape of most rising bubbles is the spherical cap, the custom drag law had to be modified, Xia *et al.*^[39] proposed a suitable drag law to describe the change of bubble shape as it grows. C_D is expressed as follows:

$$C_D = \frac{2}{3} \left(\frac{Eo}{3} \right)^{1/2}. \quad [10]$$

Eo is the Eotvos number, which is a dimensionless number describing the shape of bubble, given as follows:

$$Eo = \frac{g(\rho - \rho_b)d_b^2}{\sigma}, \quad [11]$$

where g is the gravitational acceleration (m/s^2), and σ is the interfacial tension between argon and molten steel (N/m).

Due to the conservation of momentum, the increase or decrease of the bubble momentum will inevitably cause a reduction or increase of the continuous phase momentum. Thus, the two-way turbulence coupling model was employed to realize the momentum exchange between the discrete bubbles and continuous phases.^[40,41] A momentum source was added to the continuous phase momentum through the interchange terms such as the drag force in the respective momentum equations as shown in the following equation:

$$F_b = - \sum_i^{N_{b,cell}} (F_{VM,i} + F_{D,i} + F_{P,i}) \cdot m_b \Delta t, \quad [12]$$

where $N_{b,cell}$ is the number of bubbles in a particular cell, m_b is the mass flow rate of bubbles, and Δt is the time step.

The turbulent dispersion of the bubbles was implemented by using a stochastic tracking (random walk) model to ensure an accurate representation of the bubble plume. In this model, a fluctuating component is added to the mean fluid velocity implemented in Eq. [8] to simulate turbulent fluctuations that would affect bubble motion. The fluctuating component was calculated according to the local level of turbulent kinetic energy as follows:

$$u_b = \bar{u}_b + \zeta \sqrt{2k/3}, \quad [13]$$

where \bar{u}_b is the mean fluid velocity, $\zeta \sqrt{2k/3}$ is velocity fluctuation term, and ζ is a random number uniformly distributed between 0 and 1.

3. Bubble size model

Spherical-cap bubbles were injected, respectively, from the ladle bottom and up-snorkel for SSRF and RH, and the shape factor was set to 0.7.^[42] The interactions between gas bubbles, such as coalescence and breakup, were ignored.^[43,44] When bubbles were injected from the nozzle, the initial diameter of the bubble was calculated by the following experimental formula^[45,46]:

$$d_{b,0} = 0.091 \left(\frac{\sigma}{\rho_l} \right)^{0.5} u_{b,0}^{0.44}, \quad [14]$$

where $u_{b,0}$ is injection velocity of the discrete bubble at the exit of the nozzle (m/s), σ is the surface tension (N/m), and ρ_l is the density of the liquid phase (kg/m^3).

During the process of bubble rising, the bubble density is decreased on account of the pressure drop. To describe this expansion process, the density and diameter of the rising bubble were calculated at each time step according to the ideal gas law^[47,48]:

$$\rho_{b,0} = \rho_{Ar} \frac{(P_V + P_{b,0}^{st}) T_0}{P_0 T_l} \quad [15]$$

$$\rho_{b,t} = \rho_{b,0} \frac{P_V + P_{b,t}^{st}}{P_V + P_{b,0}^{st}} \quad [16]$$

$$d_{b,t} = d_{b,0} \left(\frac{\rho_{b,0}}{\rho_{b,t}} \right)^{1/3}, \quad [17]$$

where $\rho_{b,0}$ is the initial bubble density at the exit of nozzle (kg/m^3), P_0 and T_0 are standard temperature and pressure (STP), 101325 Pa and 298.15 K. P_V is the pressure in vacuum chamber, and ρ_{Ar} is the argon density at condition of STP. T_l is the temperature of

molten steel, 1873 K. $P_{b,0}^{st}$ and $P_{b,t}^{st}$ are the static pressure of liquid steel at ladle bottom and rising height of bubble, respectively. With the help of user-defined functions (UDFs) in the Ansys software, the updated values of density ($\rho_{b,t}$) and diameter ($d_{b,t}$) are returned to solve the trajectory equation of bubble at each time step.

4. Boundary and initial conditions

The grid of fluid domain and boundary conditions are shown in Figure 4, in which the whole domain was divided into four parts, depending on the initial distribution of fluid at vacuum pressure. The local refinement of the grid was applied at the phase interfaces and high-velocity plume region. The walls of the ladle, snorkel, and vacuum chamber were set to be no-slip wall function. The pressure-outlet boundary condition was adopted on the top surface of the vacuum chamber and ladle. Initially, four fluid zones were filled with the corresponding fluid, and then the bubbles were injected from the nozzle. Finally, bubbles disappear after arriving at the interface where the volume fraction of the continuous gas phase is more than 0.5.

5. Simulation method

The software of ANSYS-Fluent® 17.0 was used, combining with user-defined functions (UDFs) to solve the multiphase flow. Figure 5 shows the detailed solution procedure of the current model. The PISO algorithm was used to achieve the pressure-velocity coupling scheme, and the hybrid parallel computing was

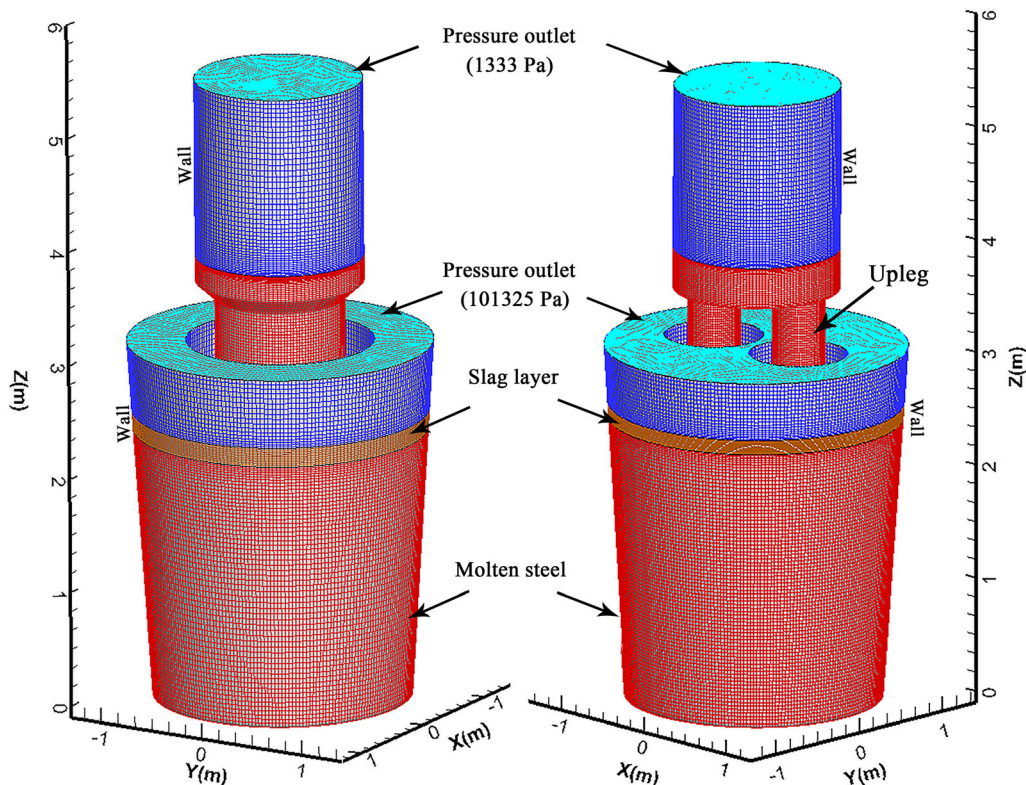


Fig. 4—Computational domain and mesh of 80t-SSRF and RH.

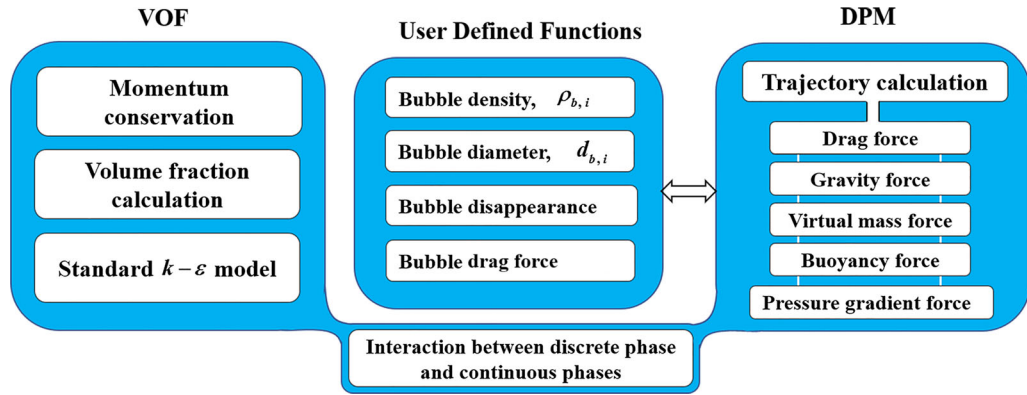


Fig. 5—The solution schematic of the coupled VOF-DPM with user-defined functions.

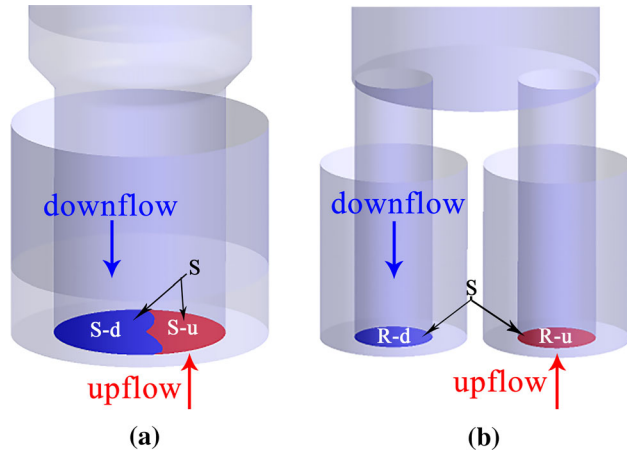


Fig. 6—The location of the test surface for the calculation of circulation rate in: (a) SSRF, (b) RH.

performed in all calculations. The tolerance for the normalized residuals error per iteration was less than 10^{-3} for all variables. After initialization, the transient simulation was run until a quasi-steady state was achieved. All the calculations were performed on a platform of Intel Xeon E5-2697 3.4 GHz with 32 GB RAM.

6. Determination of circulation rate and mixing time

The circulation rate was defined as the mass exchange rate of steel between ladle and snorkel. As shown in Figure 6(a), the cross section at the exit of the snorkel was selected as the test surface (S) to calculate the circulation rate in SSRF. Since the upflow and downflow coexist in the snorkel, the surface-S was divided into two portions (S-u and S-d) according to the positive and negative of vertical steel velocity, corresponding to the area occupied by the upflow and downflow, respectively. For RH system, as shown in Figure 6(b), the cross sections (R-u, R-d) at the exit of up- and down-snorkel were selected as the test surface to calculate the circulation rate of upflow and downflow, respectively. The mass flow rate through the specified area was computed as follows^[31]:

$$M = \sum_{i=1}^n \rho_l \cdot u_i^z \cdot A_i, \quad [18]$$

where n is the mesh number at the surface, A_i is the projected area of a cell at the surface, and u_i^z is the vertical velocity of steel. Two criteria are adopted to assess whether the “quasi-steady state” is reached in the model: (i) the net mass flow rate of steel on the surface-S is close to zero because of mass conservation; (ii) for the mass flow rate of upflow and downflow (M_{up} , M_{down}), their values keep relative stable, respectively.

The mixing time was calculated by solving the species transport equation:

$$\frac{\partial}{\partial t}(\rho_m C) + \nabla \cdot (u_m \rho_m C) = \nabla \cdot \left[\frac{\mu_m + \mu_t}{Sc} \left(\frac{\partial C}{\partial x_i} \right) \right], \quad [19]$$

where C is the tracer concentration, and Sc is the turbulent Schmidt number which is set to 0.7.^[33] The tracer species is assumed to be chemically inert, having the same physical properties as liquid steel. The 95 pct mixing time is quantified as the monitoring value within ± 3 pct of final concentration (C_∞).

III. RESULTS AND DISCUSSION

A. Model Validation

To validate the mathematical model, cold experiments and numerical simulations were conducted in air–water systems. The calculated mixing time was compared with the measured results using the electrical conductivity sensor. The concentration signal as a function of time was recorded on a computer. The criterion to judge mixing time was the value of 97 pct homogenization. Figure 7 shows the typical curves of measurement dimensionless conductivity with time at three monitored points in the SSRF system. The large discrepancy among curves implies that the local mixing times at three points are different, the longest time is at P3. This result agreed well with the reported works of literature that the dead zone of flow is located normally at the periphery of the snorkel for both reactors.^[31,48,49] Each

test was repeated five times to ensure the reliability of the results, and the average value was adopted as the final mixing time. Figure 8 shows the comparison of predicted mixing time with the measured average values. It can be found that predicted values are close to the measured values for both of reactors.

Besides that, the circulation rate of water in RH was measured using the method proposed by Seshadri and Costa.^[40] In this procedure, the KCl solution was injected from up-snorkel as a pulse, and its concentration in the down-snorkel was continuously monitored. Figure 9 shows the typical curve of concentration vs time, the circulation time is the ratio of $A/\Delta C$, where ΔC is the increment in tracer concentration after stabilization, and A is the area under the first peak of the curve. The circulation rate is estimated using the following equation^[50,51]:

$$M_C = \frac{W}{A/\Delta C}, \quad [20]$$

where M_C is the circulation rate of water, and W is the total mass of water contained in the vessel. For each condition, the average of five measurements was taken as the final circulation rate.

Figure 10 shows the comparison of predicted and measured circulation rate with the increase of gas flow rate. It is observed that the measured values of the circulation rate are relatively consistent with the predicted by the model in RH. Moreover, it can be seen that the circulation rate in SSRF is higher than in RH, which will be discussed later.

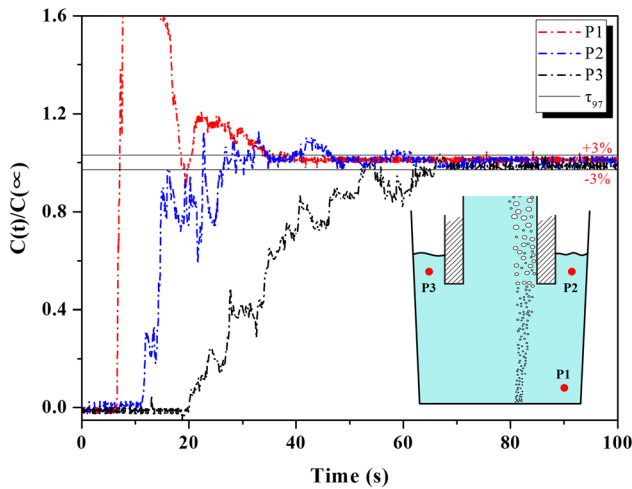


Fig. 7—The typical curves of measurement conductivity with time in the air-water system of SSRF.

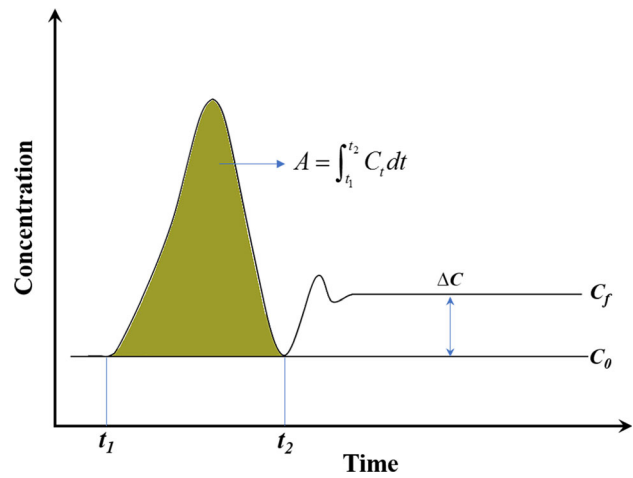


Fig. 9—Typical curve of concentration with time for calculation of circulation rate in the RH.

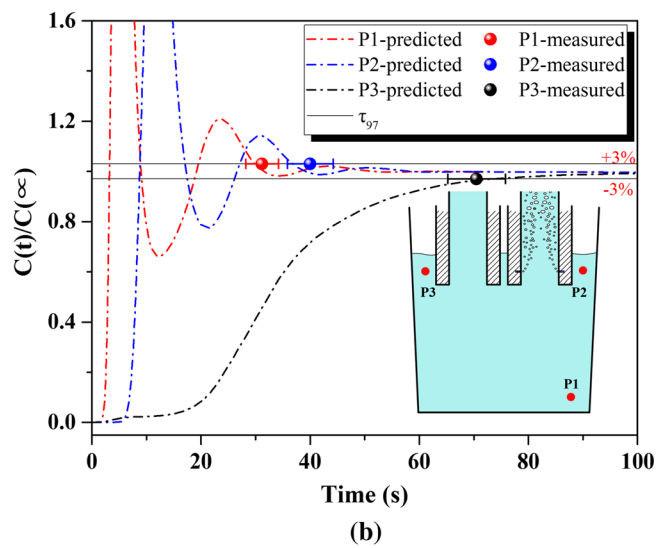
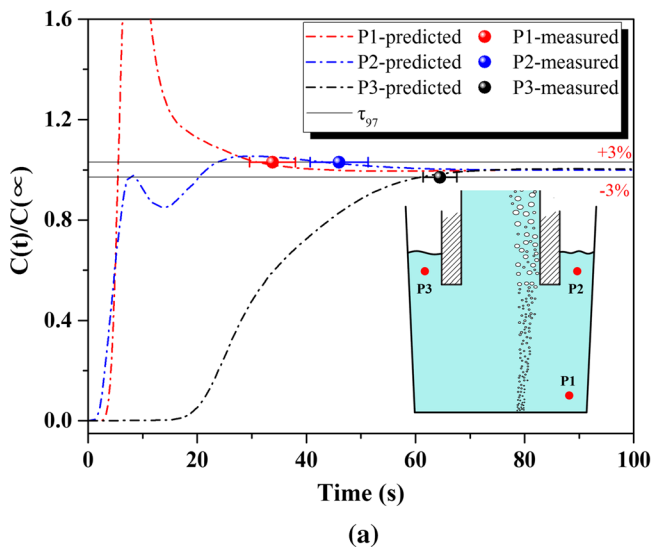


Fig. 8—The comparison of predicted 97 pct mixing time with the measured value in (a) SSRF, (b) RH.

B. Comparison of Circulation Mode

In this section, the numerical calculations were performed to investigate the differences in flow fields and evaluate the circulation capacity of liquid steel in the full-scale models of SSRF and RH. Figure 11 shows the velocity field and phase distribution in argon-steel systems of SSRF and RH at the $Y = 0$ plane. As shown in Figure 11(a), the molten steel is lifted into the vacuum chamber from up-snorkel by sidewall gas injection.

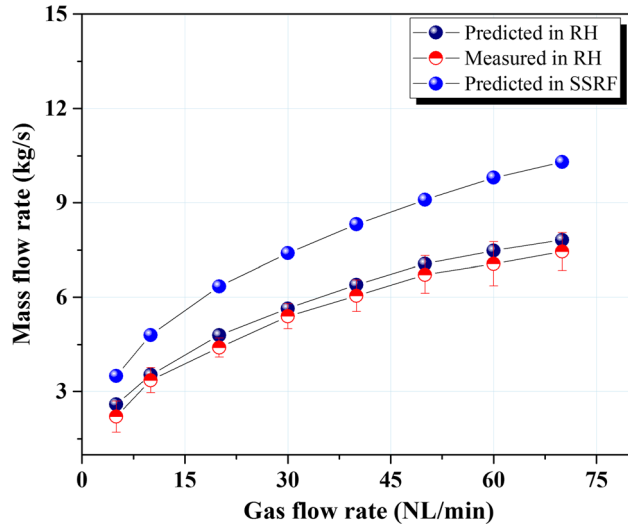


Fig. 10—Circulation rate as a function of gas flow rate in the air–water system.

After that, it flows back to the ladle through the down-snorkel with a high velocity and vertically impinges to the ladle bottom. With the obstruction of the ladle sidewall, some eddies are formed around the bottom downflow. Subsequently, the molten steel is sucked into the up-snorkel again, and the continuous circulation is built. The current predicted flow field and phase distribution in RH match well with many published results.^[42,52,53]

For the SSRF system, similar eddies are generated after the downflow impinging the ladle bottom, but the flow field in the snorkel is different from RH. The upflow and downflow are formed simultaneously in a large snorkel. The upflow is directly driven by bubble plume along the right-side wall of the snorkel. After reaching a certain height in the vacuum chamber, the molten steel falls back into the snorkel. Meanwhile, a large vortex is formed in the upper area of snorkel because of the reversal of the flow direction of molten steel. Furthermore, it is found that the velocity of downflow near the snorkel wall is almost vertical downward, while the oblique downward flow is presented as it approaches the upflow. This phenomenon indicates that not all molten steel in the downflow is completely discharged from the snorkel; a part of molten steel enters the upflow and is re-lifted into the vacuum chamber by bubble plume.

Indeed, there is a certain similarity of flow field between RH and SSRF, but each furnace has its unique circulation characteristic. Based on the contrastive analysis of the flow field, two different circulation modes can be summarized in Figure 12. For the RH

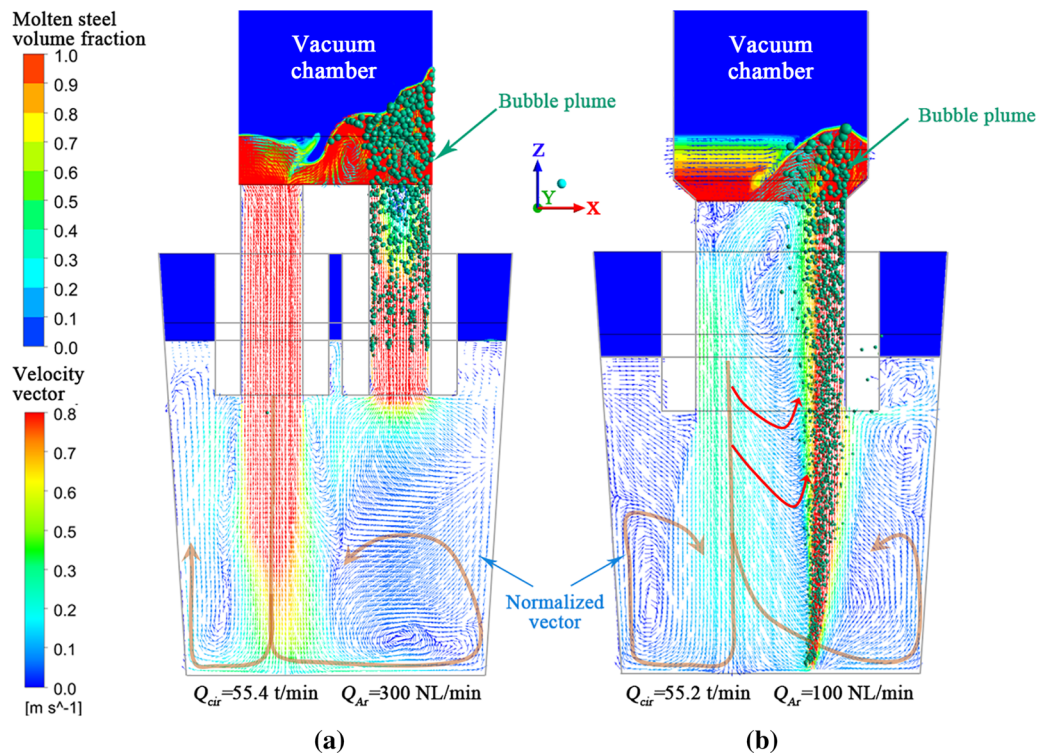


Fig. 11—Comparison of the velocity vector and phase distribution at the $Y = 0$ plane under the same circulation rate between: (a) RH, (b) SSRF.

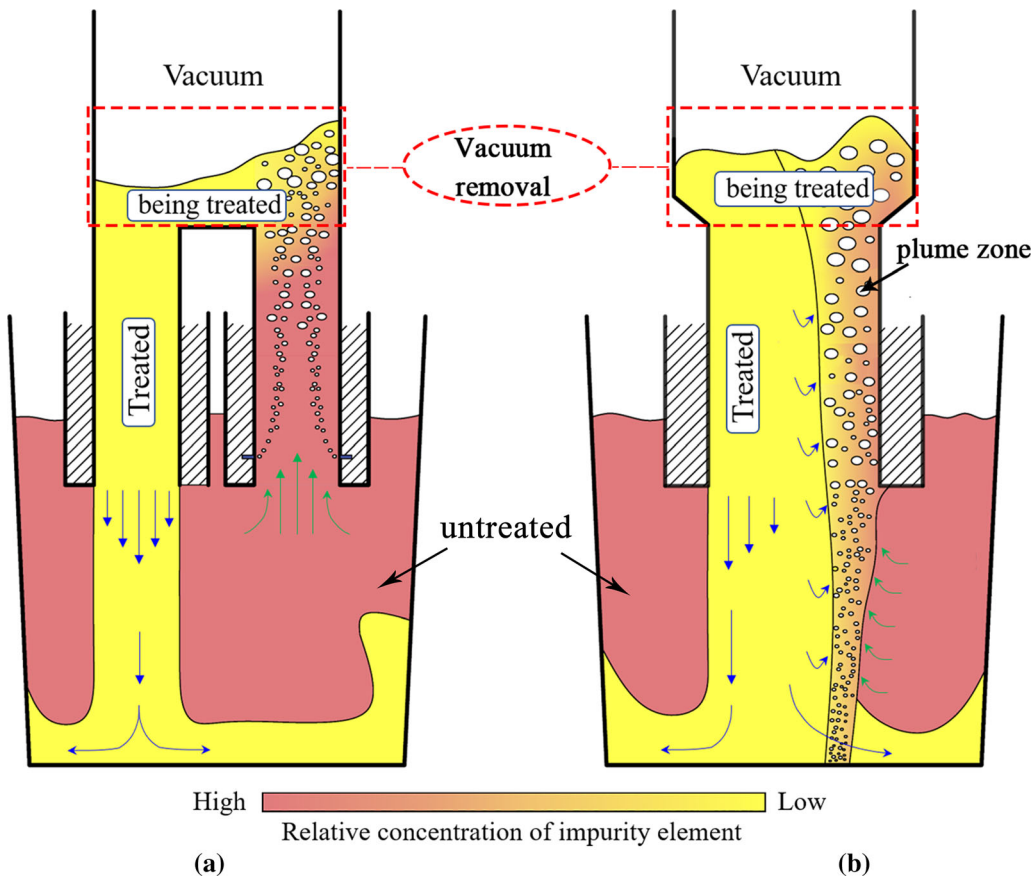


Fig. 12—The schematic diagram of steel circulation mode in vacuum reactors: (a) RH, (b) SSRF.

system, the full circulation mode is depicted in Figure 12(a); the untreated steel in the ladle is lifted into the vacuum chamber, in which some dissolved impurity elements, such as C, N, and H, can be removed with the help of vacuum circumstance. After that, all the treated molten steel directly rushes to the ladle bottom and mixes with the untreated molten steel in ladle. With this, a full cycle of molten steel is finished, and the next cycle begins. After such a few turns, the concentration of impurity elements is gradually reduced to the target content. For the SSRF system, the halfway circulation mode is depicted in Figure 12(b). After the molten steel is treated in the vacuum chamber, most of the treated steel rush obliquely towards the ladle bottom, while a portion of the treated steel is dragged into the plume zone before touching the bottom, and then lifted again into the vacuum chamber for next treating. As a result, this part of the molten steel may take a few cycles before returning to ladle or touching the bottom.

Generally, the circulation rate is regarded as a key indicator to evaluate the circulation efficiency in the SSRF and RH. Figure 13 shows the variation of the real-time value of the mass flow rate with time on test surfaces (as depicted in Figure 6). For the RH system, the mass flow rates of upflow and downflow were, respectively, monitored at surface R-u and R-d, and the net flux of molten steel is the sum of the two. For the SSRF system, the net flux was monitored at surface-S.

The flow rate of upflow and downflow cannot be monitored in real time because of changing areas of S-u and S-d with time. Thus, their values were extracted every ten seconds, according to Eq. [18]. Although the structures of the two reactors are different, the dynamic mass flow rate shows consistent evolution characteristics in Figure 13. Initially, the static fluid in up-snorkel is suddenly lifted by gas injection, resulting in an imbalance pressure field between inside and outside of the vacuum chamber. To recover balance, the liquid steel in the vacuum chamber is discharged through the down-snorkel. Therefore, the predicted net flux shows a dramatical oscillation at first, but the amplitude decreases with time until the circulation approaches quasi-steady state, where the net flux closes to zero, and the mass flow rate of upflow or downflow keeps stable. With this, it is judged that the quasi-steady flow state is achieved after about 60 seconds for both reactors.

In light of this judgment criteria, the effect of gas flow rate on the circulation rate was investigated. Figure 14 shows the comparison of the circulation rate between SSRF and RH with the increasing gas flow rate. The result indicates that the circulation rate of SSRF is much higher than that of RH as the same gas flow rate is injected. It implies the SSRF shows the higher utilization degree of lifting gas. In the RH process, the lifting gas is injected from up-snorkel at a shallow depth below the vacuum steel surface, while the lifting gas of SSRF is

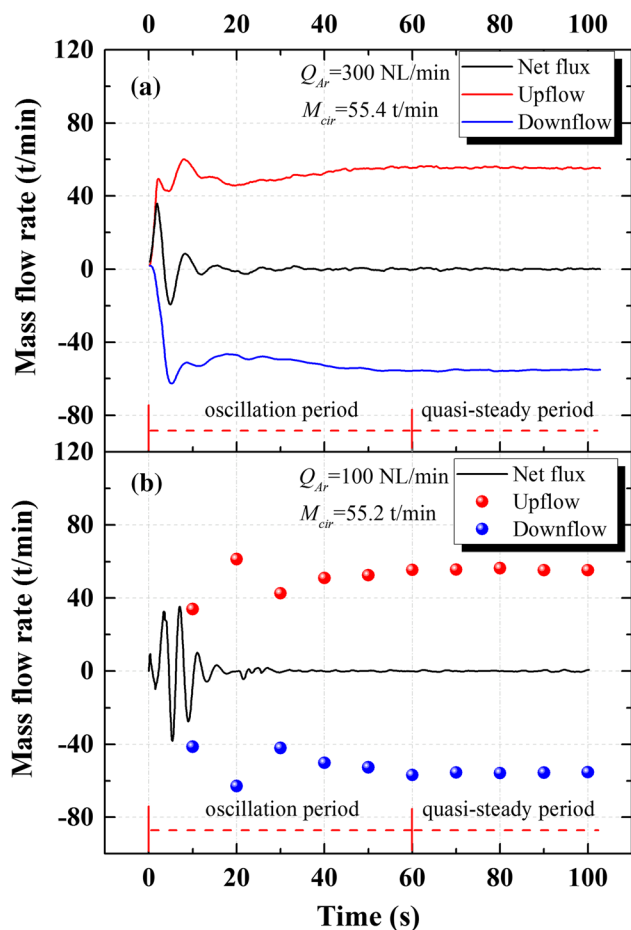


Fig. 13—The variation of real-time monitoring value of mass flow rate with time in (a) RH, (b) SSRF.

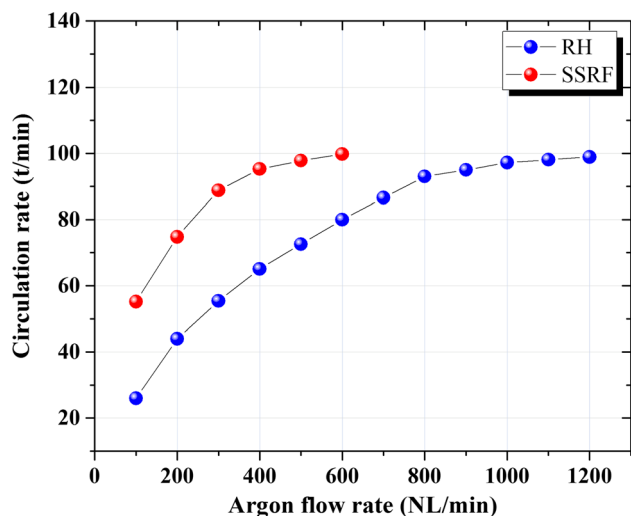


Fig. 14—Circulation rate as a function of gas flow rate in the argon-steel system.

injected from ladle bottom with large depth. All the energy required for circulation is provided by the bubble's floating, whether in RH or SSRF. The larger injection depth means the bubbles need to experience

longer floating distance and time in molten steel. As a result, the gas contributes more stirring power for steel circulation.

C. Oil/Water Behavior

Based on the above analysis of flow field, the flow behaviors of top slag in the vacuum chamber were further investigated in this section. The cold experiments were performed, respectively, in RH and SSRF by use of the setup, as presented in Figure 3. The differences in water level and immersion depth of snorkel were controlled and kept constant in all the experiments. The results of numerical calculations were adopted to ensure the circulation at the same level between two reactors. As presented in Figure 10, the gas flow rate of 20, 40, 60 NL/min are required, respectively, in RH to achieve the almost same circulation rate as SSRF at the gas flow rate of 10, 20, 30 NL/min. For each experiment, the initial thickness of *N*-pentane oil layer was controlled to 6 mm (about 750 mL) in the vacuum chamber before gas injection; after the pressure stabilization, the argon was injected, and the movement process of slag droplets in water was recorded simultaneously.

1. Observation in RH

Figure 15 shows the image sequence of oil movement in the vacuum chamber and down-snorkel. At the beginning (2 seconds), the water level above the up-snorkel is suddenly raised by rising bubble plume, and the top oil layer is pushed to the left side. Because of the violent oscillation of the water level, the strong turbulence is formed at the interface of oil/water. As a result, many oil droplets were created and entrained in the lower water phase. After about 4 seconds, the raised water level recovers to the original height, and the water wave repeatedly propagates from right to left along with the water level. It is clear at moments of 10 and 14 seconds, once the wave encounters the oil layer, the oil droplets are formed below the wave. Eventually, all these droplets are dragged into the down-snorkel, accompanying the downward water flow.

Figure 16 shows the distribution of the droplets in ladle for different gas flow rates. As shown in Figure 16(a), the downflow, mixed with the droplets, rushes towards the ladle bottom. In the initial stage of the descent process, the movement of oil droplets is dominated by high-velocity downflow. After reaching a certain depth, self-buoyancy becomes dominant, and the droplets begin to float towards the free surface of the ladle. As a result, many droplets accumulate on the free surface, and the new oil layer is formed and extended to the entire surface in the ladle. It worth noting that only very few droplets are sucked into the up-snorkel and lifted into the vacuum chamber. After about 50 seconds, all the top oil layer is almost drained in the vacuum chamber. With the increase of gas flow rate, the output of droplets is increased on account of the stronger level oscillation and the faster water circulation. As expected, more droplets are generated and dragged into the ladle,

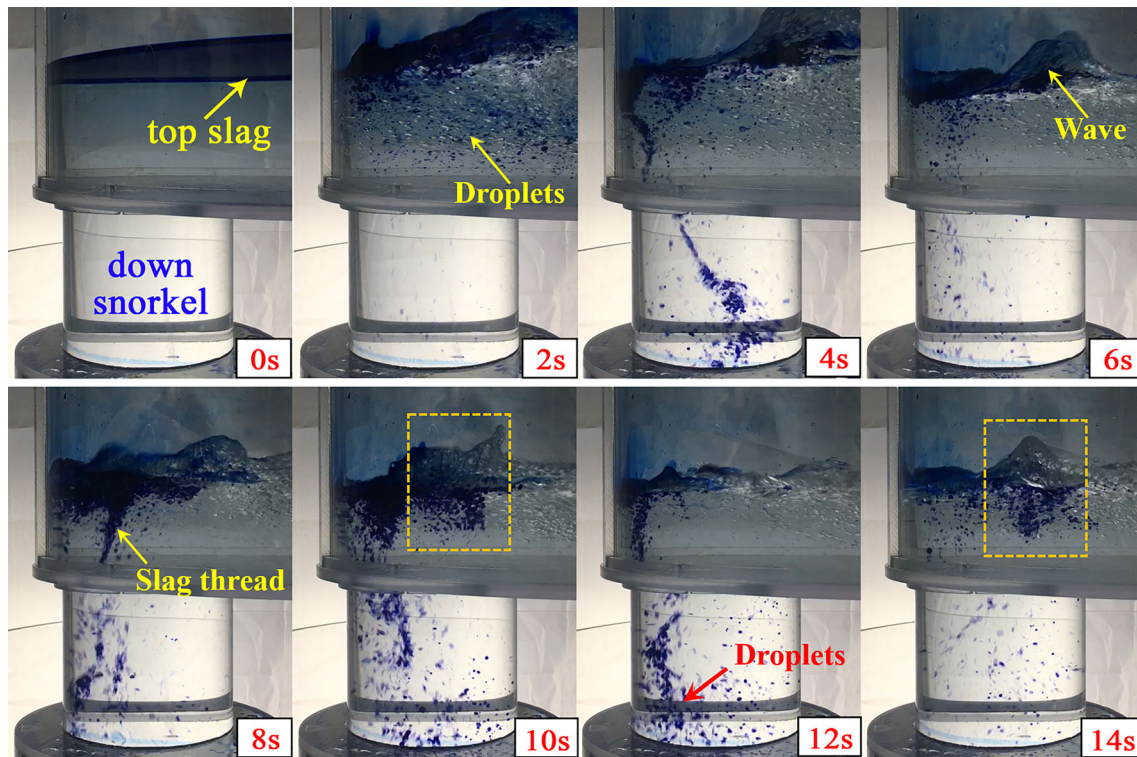


Fig. 15—The image sequence of slag movement in the vacuum chamber and down-snorkel of RH (20 NL/min).

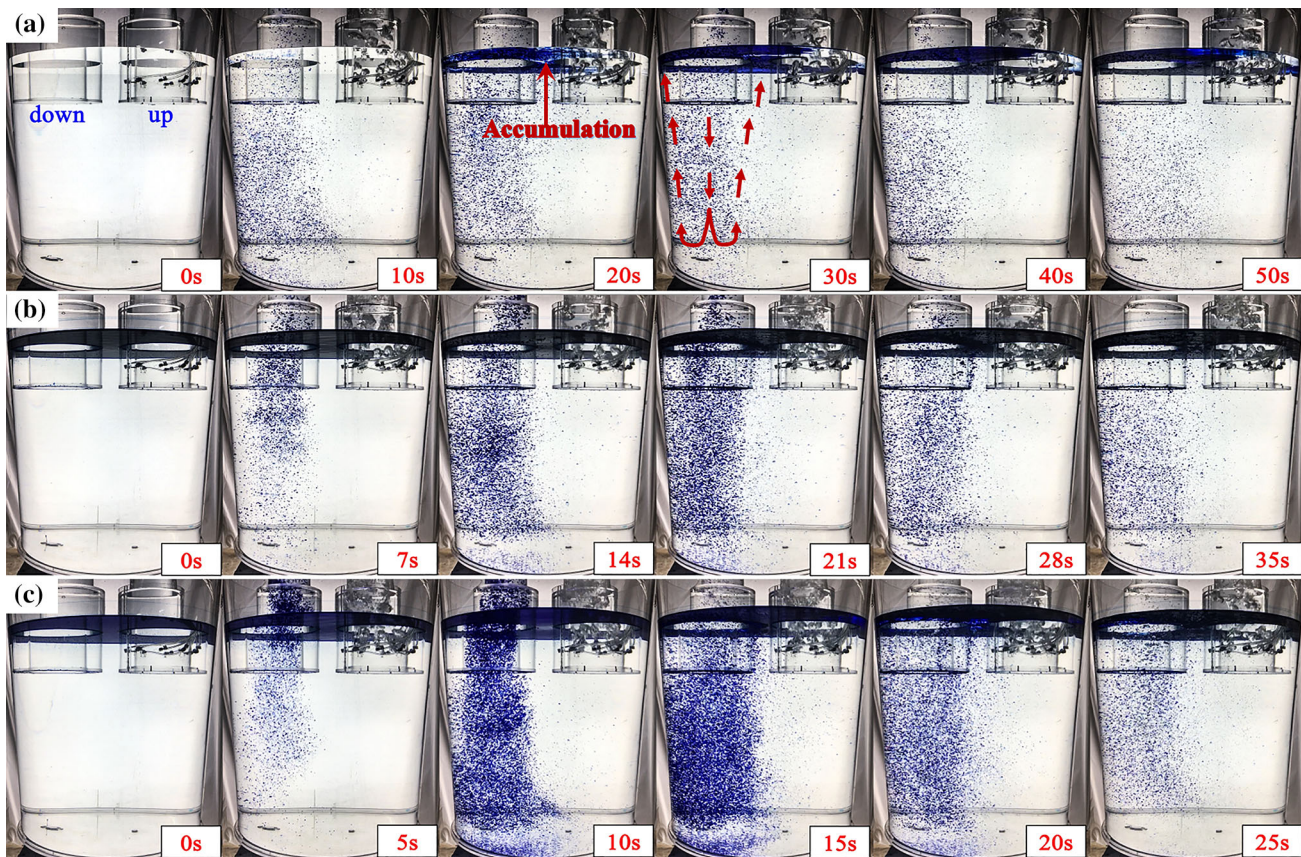


Fig. 16—The image sequence of slag movement in ladle of RH under different gas flow rates: (a) 20 NL/min, (b) 40 NL/min, (c) 60 NL/min.

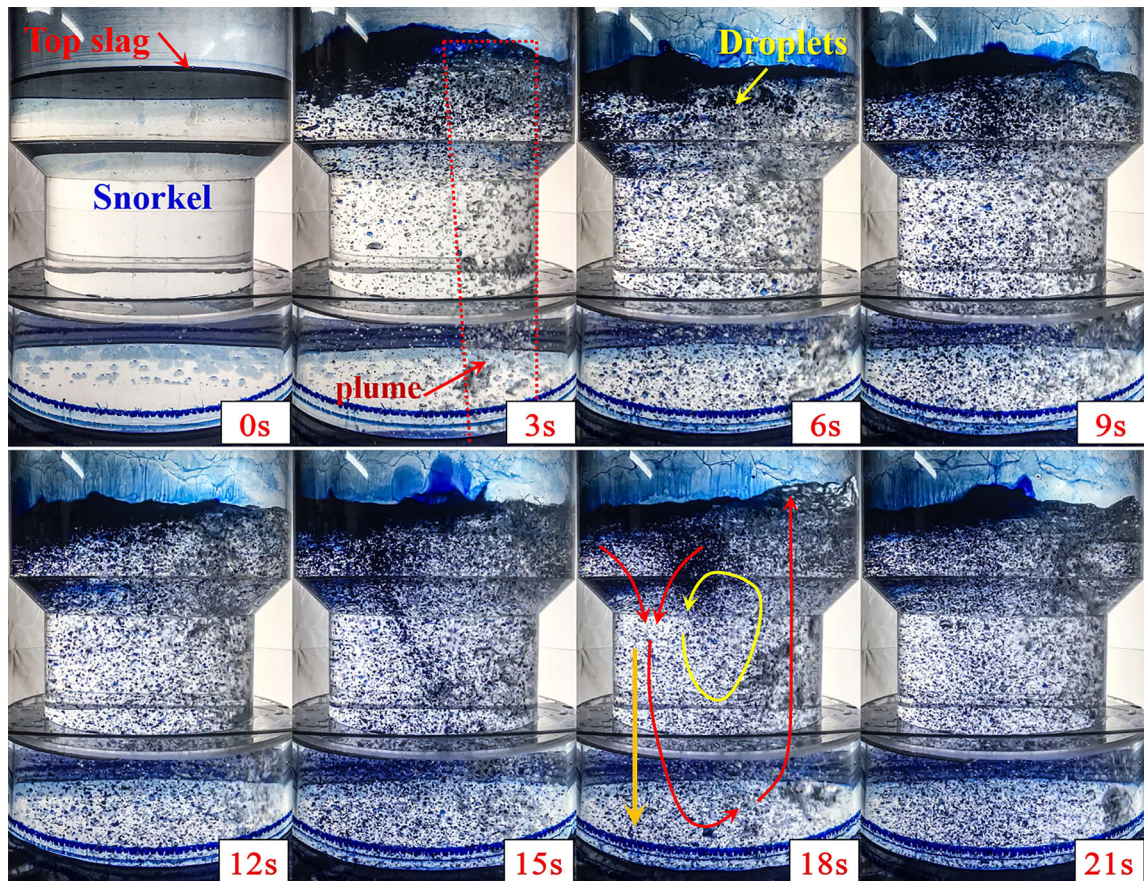


Fig. 17—The image sequence of slag movement in the vacuum chamber and snorkel of SSRF (30 NL/min).

and the time required for draining all oil layer is reduced, respectively, to 35 and 25 seconds, corresponding to the gas flow rate of 40 and 60 NL/min.

2. Observation in SSRF

Figure 17 shows the visualized distribution of oil droplets in the vacuum chamber and the snorkel of SSRF. It can be found that a good deal of oil droplets appears below the interface of the oil/water. Just like RH, these droplets can also be captured and then dragged into the lower position by the downward stream. However, during the descending process, the motion trail of droplets is different from RH. As mentioned before, the movement of oil droplet is easily dominated by rapid water flow. Depending on the unique flow pattern as presented in Figure 11(b), three types of trajectories were observed from the image sequence. The first is almost vertical movement; oil droplets near the left snorkel wall are directly dragged into the ladle. The second is local rotation; some droplets are captured by a local vortex, in which movement of droplets are constrained, resulting in a long-time rotation and stop in the vortex. The third is large circulation; owing to the sloping flow field of downflow, some of the descending droplets gradually approach the upflow, and then captured by rising bubble plume. As a result, they are lifted into the vacuum chamber, and then merged into the top oil layer.

Figure 18 shows the oil droplet distribution after entering the ladle. It can be found that the third-type movement not only exists in the snorkel even extends into the ladle. After a short stay, most of the droplets are lifted again to the snorkel by bubble plume. During the lifting process, a small number of oil droplets are led out of the snorkel together with the few bubbles, and then float up to the free surface. As shown in Figure 18(a), after about 50 seconds, the amount of accumulation at the free surface is far less than RH. With the increase of circulation rate, more droplets are generated and circulated between snorkel and ladle, and more oil droplets float to the free surface. Despite this, there are still many oil droplets staying in the water at the high circulation rate, as shown in Figure 18(c). Besides that, a common phenomenon was found that most of the moving droplets are concentrated in the inner and lower regions of the snorkel, and would not easily spread to other places in the ladle.

3. Contrastive analysis of slag-metal behavior

Based on the above observation of cold experiments, the flow mechanism of top slag in RH and SSRF can be depicted as Figure 19. Some common and different behaviors can be summarized as follows. They have in common that the intense turbulence shreds the slag layer

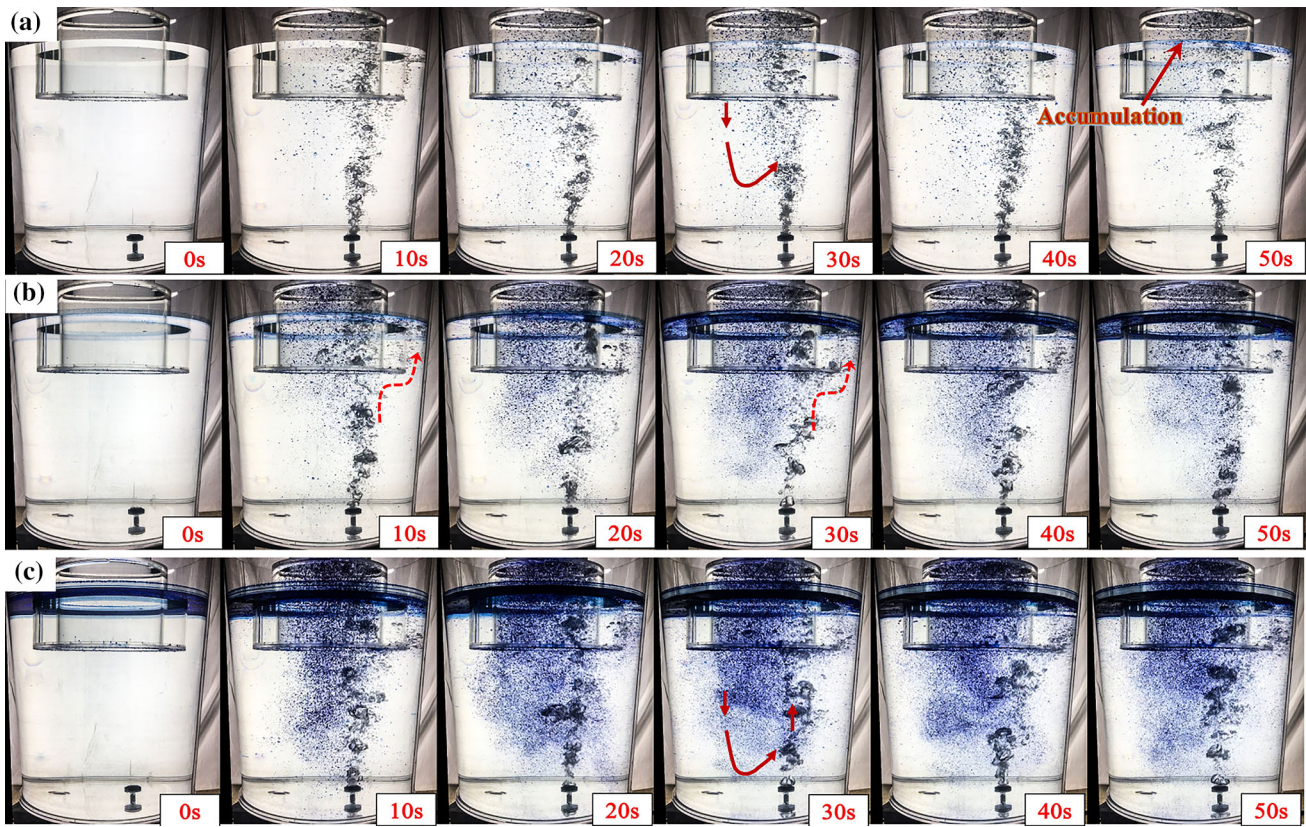


Fig. 18—The image sequence of slag movement in ladle of SSRF under different gas flow rates: (a) 10 NL/min, (b) 20 NL/min, (c) 30 NL/min.

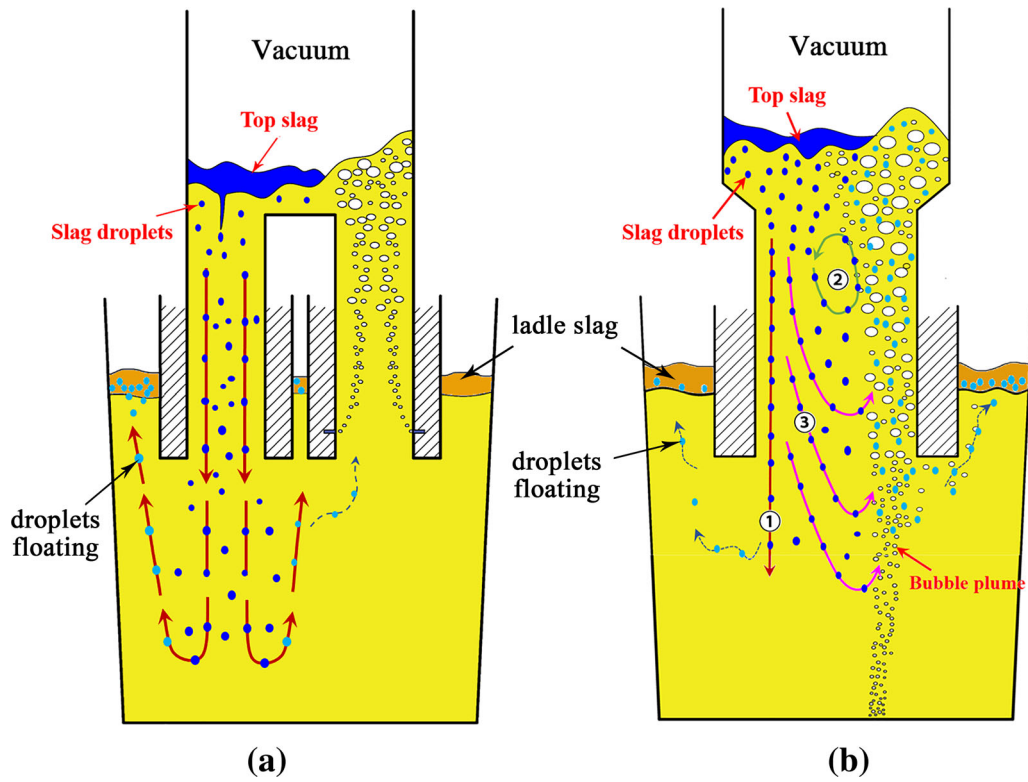


Fig. 19—The schematic diagram of the slag droplets movement in (a) RH, (b) SSRF.

into fine droplets in the vacuum chamber, and strong circulation allows the droplets to be quickly diffused into the molten steel and in full contact with it. If the top slag is added as a desulfurizer in the real situation, it means that the desulfurization reaction not only occurs at the interface of the slag layer and the molten steel but also rapidly spreads to the contact surface between slag droplets and steel. Thus, the desulfurization rate is greatly increased. Nevertheless, some of the differences between them are also found. As shown in Figure 19(a), the trajectory of the slag droplets is relatively uniform in RH, that is, descending from the vacuum chamber to the ladle, and then floating up to the free surface. However, three trajectories are formed in SSRF as discussed before. It can be found in Figure 19(b) that the majority of droplets are continuously circulated among the vacuum chamber, snorkel, and the ladle. Only a small part of the droplets floats directly into the ladle slag. More importantly, in the actual process, the ladle slag is usually covered above the surface of molten steel, which means that the floating droplets will eventually merge into the ladle slag. Some slag droplets may not have completely reacted before entering the ladle slag, especially under the condition of a high circulation rate. Once these slag droplets enter the ladle slag, their desulfurization function fails. On the whole, the flow pattern of slag droplets in SSRF is more conducive to long-time contact between desulfurizer and molten steel, and the utilization rate of desulfurizer may be higher in SSRF.

D. Industrial Tests

Industrial tests were carried out to validate and compare the differences in refining effects caused by two different movement mechanisms of slag droplets. In a steel plant, the BOF (Basic Oxygen Furnace) → RH → CC (Continuous Casting) process route was adopted to produce non-oriented electrical steels, which has strict requirements of carbon content (< 30 ppm) and sulfur content (< 40 ppm). An 80-ton SSRF was built through the modification of 80t-RH, and two snorkels of RH were replaced by a large-size snorkel and connected with the vacuum chamber. The lifting gas was blown from

ladle bottom by a porous brick. During the tapping of BOF, the molten steel was not deoxidized to remain high oxygen potential for next decarburization. For vacuum treatment, the decarburization was firstly performed in the vacuum reactor. After the decarburization, aluminum deoxidation, and alloying steps are completed in sequence, the pre-melted slag [w(CaO):w(CaF₂) = 3:1] was added from vacuum chamber to carry out the desulphurization task. Apart from the argon flow rate, other technological parameters are consistent for two reactors, such as vacuum pressure and snorkel immersion depth. The actual argon flow rates, 1100 and 350 NL/min, were blown for RH and SSRF, respectively. As predicted by the numerical simulation in Figure 14, these two argon flow rates can achieve the almost same level of circulation rate. Two kinds of slag addition, *i.e.*, 600 and 400 kg, were conducted for each reactor. A total of 12 heats were smelted; RH and SSRF each performed six heats. Before vacuum treatment, the initial conditions of incoming molten steel for each heat are listed in Table III.

Table IV shows content evolution during the vacuum process. It can be found that both reactors show an equal decarburization capacity, that is, the carbon content is decreased from 200-350 to 20-30 ppm. This result indicates that both of the two circulation modes enable rapid circulation and vacuum removal of impurity from molten steel.

Figure 20 shows the comparison of the desulphurization degree between SSRF and RH. For the condition of 600 kg addition, the average desulfurization degree is increased from 46.7 pct in RH to 74.6 pct in SSRF. However, with the decrease of slag addition, the desulfurization degree is declined for both of them; the SSRF shows an average 66.9 pct desulfurization capacity, which is still higher than 32.3 pct in RH. As the results of the physical model have explained, in the SSRF process, the slag droplets can be circulated repeatedly between ladle and snorkel owing to its unique circulation flow. Consequently, the desulfurizer is fully reacted with the sulfur dissolved in molten steel. In terms of endpoint sulfur content, it is clear in Table IV that the terminal sulfur content can be stably

Table III. Initial Conditions of Incoming Molten Steel for Vacuum Treatment

Reactor	Heat No.	Melt Weight /ton	Slag Thickness /mm	T ₀ /°C	[C] ₀ / pct	[O] ₀ /ppm
RH	1-1	85.2	100	1647	0.0341	714
	1-2	86.8	90	1617	0.0309	753
	1-3	83.5	80	1604	0.0257	673
	1-4	85.1	80	1598	0.0232	546
	1-5	84.5	70	1626	0.0325	705
	1-6	86.1	90	1620	0.0267	615
SSRF	2-1	85.5	80	1640	0.0252	725
	2-2	82.8	100	1616	0.0266	597
	2-3	85.2	110	1642	0.0227	812
	2-4	83.6	80	1635	0.0325	606
	2-5	84.3	90	1637	0.0353	622
	2-6	84.1	100	1623	0.0313	578

Table IV. Refining Operations and Component Evolutions

Reactor	Heat No.	Argon Flow Rate /NL·min ⁻¹	After Al-Deoxidation				Terminus	
			T ₁ /°C	[S] ₀ /ppm	[Al] / pct	Slag Addition /kg	[C] _T /ppm	[S] _T /ppm
RH	1-1	1100	1610	58	0.260	600	24	30
	1-2	1100	1599	61	0.250	600	26	32
	1-3	1100	1613	52	0.240	600	27	29
	1-4	1100	1570	54	0.270	400	27	37
	1-5	1100	1582	52	0.240	400	25	35
	1-6	1100	1593	55	0.250	400	22	36
SSRF	2-1	350	1600	60	0.270	600	21	16
	2-2	350	1588	57	0.240	600	24	15
	2-3	350	1598	52	0.250	600	23	12
	2-4	350	1589	54	0.260	400	25	17
	2-5	350	1615	60	0.240	400	27	20
	2-6	350	1584	61	0.250	400	23	21

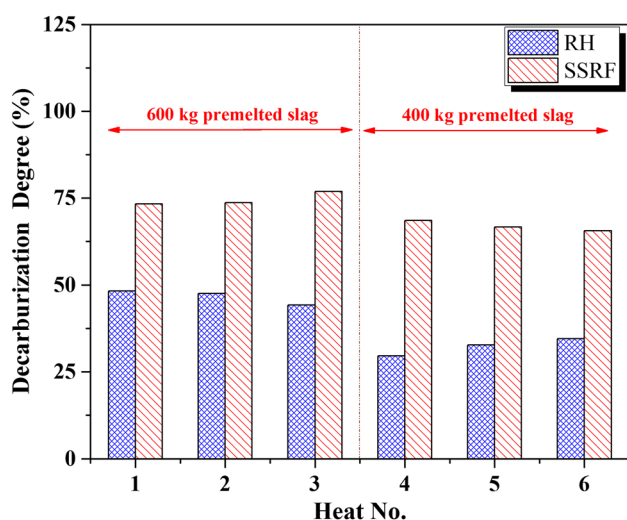


Fig. 20—Comparison of desulphurization degree in industrial tests.

controlled to below about 20 ppm in SSRF, far below the target of 40 ppm, and the minimum can reach 12 ppm.

IV. CONCLUSIONS

In this study, a method of combining numerical modeling with water modeling was used to clarify the formation mechanism of the slag droplet behavior. Then the industrial test successfully verified that strong desulfurization capacity was realized in SSRF owing to the circulating flow of slag droplets. Based on results and discussion, the following conclusions can be drawn.

1. The reliability of the current mathematical model has been validated using cold experiments. The predicted results of the mixing time and circulation rate agreed well with the measured results, indicating that the multiphase flow of the argon-steel system can be described reasonably using the current model.

2. Depending on the analysis of the flow field, it was found that the circulation mechanism of molten steel in SSRF is different from RH. For each circulation cycle, the treated molten steel in RH is exchanged fully between the vacuum chamber and ladle, while the halfway exchange was presented in SSRF due to the interaction between the reverse streams.
3. Compared with the RH, the less lifting gas is needed in SSRF to achieve an equivalent level of circulation rate owing to its tremendous injection depth.
4. The flow behaviors of top slag were compared between SSRF and RH, and the main difference is that the dispersed slag droplets can be circulated repeatedly in SSRF accompanying with the circulation of molten steel. In terms of contact reaction, the circulating flow of slag droplets will be more helpful in the full reaction of slag-steel.
5. The results of industrial tests show that compared with traditional RH, the higher desulphurization degree could be achieved by the use of SSRF with less consumption of lifting gas and desulfurizer.

ACKNOWLEDGMENT

The authors express thanks to the National Natural Science Foundation of China (Grant Nos. 51674024 and 51874034) for financial support.

REFERENCES

1. J. Zhang: *Dali. Spec. Steel*, 1978, vol. 3, pp. 5–26.
2. G.G. Cheng, Q.X. Rui, Z. Qin, and J. Zhang: *China Metall.*, 2013, vol. 23, pp. 1–10.
3. Z.M. You, G.G. Cheng, X.C. Wang, Z. Qin, J. Tian, and F. Jiang: *Metall. Trans. B*, 2015, vol. 46B, pp. 459–72.
4. K. Miyamoto, H. Aoki, and S. Kitamura: *CAMP-ISIJ.*, 1998, vol. 11, p. 756.
5. H. Aoki, H. Furuta, N. Hirashima, and S. Kitamura: *CAMP-ISIJ.*, 1998, vol. 11, p. 757.

6. H. Aoki, H. Furuta, K. Fujiwara, K. Yamashita, K. Yonezawa, and S. Kitamura: *CAMP-ISIJ*, 1998, vol. 11, p. 758.
7. H. Sugano, A. Shinkai, K. Kato, K. Miyamoto, K. Yamashita, and S. Kitamura: *CAMP-ISIJ*, 1999, vol. 12, p. 747.
8. K. Miyamoto, H. Sugano, A. Shinkai, K. Kato, S. Kitamura, and K. Yamashita: *CAMP-ISIJ*, 1999, vol. 12, p. 748.
9. M. Yano, S. Kitamura, K. Harashima, T. Inomoto, K. Azuma, and H. Nagahama: *Nippon Steel Tech. Rep.*, 1994, vol. 61, pp. 15–21.
10. S. Kitamura, H. Aoki, K. Miyamoto, H. Furuta, K. Yamashita, and K. Yonezawa: *ISIJ Int.*, 2000, vol. 40, pp. 455–59.
11. H. Aoki, S. Kitamura, and K. Miyamoto: *Iron Steelmak.*, 1999, vol. 26, pp. 17–21.
12. Z. Qin, M.T. Zhu, G.G. Cheng, and J. Zhang: *Spec. Steel*, 2010, vol. 31, pp. 5–7.
13. Q.X. Rui, F. Jiang, Z. Ma, Z.M. You, G.G. Cheng, and J. Zhang: *Steel Res. Int.*, 2013, vol. 84, pp. 192–97.
14. M.K. Mondal, N. Maruoka, S. Kitamura, G.S. Gupta, H. Nogami, and H. Shibata: *Trans. Indian Inst. Metall.*, 2012, vol. 65, pp. 321–31.
15. X.M. Yang, M. Zhang, F. Wang, J.P. Duan, and J. Zhang: *Steel Res. Int.*, 2012, vol. 83, pp. 55–82.
16. D.Q. Geng, X. Zhang, X. Liu, P. Wang, H.T. Liu, H.M. Chen, C.M. Dai, H. Lei, and J.C. He: *Steel Res. Int.*, 2015, vol. 83, pp. 724–31.
17. H. Yang, S. Yang, J. Li, and J. Zhang: *J. Iron Steel Res. Int.*, 2014, vol. 21, pp. 995–1001.
18. C. Shen, L.P. Wu, J.B. Guo, Y.W. Pan, and F. He: *Ironmak. Steelmak.*, 2019, <https://doi.org/10.1080/03019233.2019.1580029>.
19. J.H. Wei, S.J. Zhu, and N.W. Yu: *Ironmak. Steelmak.*, 2000, vol. 27, pp. 129–37.
20. M. Van Ende, Y. Kim, M. Cho, J. Choi, and I. Jung: *Metall. Trans. B*, 2011, vol. 42B, pp. 477–89.
21. C.Y. Zhu, P.J. Chen, G.Q. Li, X.Y. Luo, and W. Zheng: *ISIJ Int.*, 2016, vol. 56, pp. 1368–77.
22. S. He, G. Zhang, and Q. Wang: *ISIJ Int.*, 2012, vol. 52 (6), pp. 977–83.
23. J.M. Peixoto, W.V. Gabriel, T.S. De Oliveira, C.A. Da Silva, I.A. Da Silva, and V. Seshadri: *Metall. Trans. B*, 2018, vol. 49B (5), pp. 2421–34.
24. Z. Qin: Ph.D. Dissertation, University of Science and Technology Beijing, Beijing, China, 2010.
25. Q.X. Rui: Ph.D. Dissertation, University of Science and Technology Beijing, Beijing, China, 2012.
26. B.H. Zhu, Q.C. Liu, D. Zhao, S. Ren, and M.R. Xu: *Steel Res. Int.*, 2016, vol. 87 (2), pp. 136–45.
27. S. Yamashita and M. Iguchi: *ISIJ Int.*, 2003, vol. 43 (9), pp. 1326–32.
28. Y. Liu, M. Ersson, H. Liu, P.G. Jönsson, and Y. Gan: *Metall. Trans. B*, 2019, vol. 50B (1), pp. 555–77.
29. D. Mukherjee, A.K. Shukla, and D.G. Senk: *Metall. Trans. B*, 2017, vol. 48B (2), pp. 763–71.
30. M.S.C. Terrazas and A.N. Conejo: *Metall. Trans. B*, 2015, vol. 46B (2), pp. 711–18.
31. W. Dai, G.G. Cheng, S.J. Li, Y. Huang, G.L. Zhang, Y.L. Qiu, and W.F. Zhu: *ISIJ Int.*, 2019, vol. 59 (7), pp. 1214–23.
32. Y. Luo, C. Liu, Y. Ren, and L. Zhang: *Steel Res. Int.*, 2018, vol. 89, pp. 1–13.
33. H.P. Liu, Z.Y. Qi, and M.G. Xu: *Steel Res. Int.*, 2011, vol. 82, pp. 440–58.
34. J.U. Brackbill, D.B. Kothe, and C. Zemach: *J. Comput. Phys.*, 1992, vol. 100, pp. 335–54.
35. M. van Sint Annaland, N.G. Deen, and J.A.M. Kuipers: *Chem. Eng. Sci.*, 2005, vol. 60, pp. 2999–3011.
36. B.E. Launder and D.B. Spalding: *Lectures in Mathematical Models of Turbulence*, Academic Press, London, 1972.
37. S. He, G. Chen, and C. Guo: *Ironmak. Steelmak.*, 2019, vol. 46 (8), pp. 771–76.
38. L.M. Li, Z.Q. Liu, M.X. Cao, and B.K. Li: *JOM*, 2015, vol. 67, pp. 1459–67.
39. J.L. Xia, T. Ahokainen, and L. Holappa: *Scand. J. Metall.*, 2001, vol. 30, pp. 69–76.
40. H.T. Ling, F. Li, L.F. Zhang, and A.N. Conejo: *Metall. Trans. B*, 2016, vol. 47B, pp. 1950–61.
41. S.W.P. Cloete, J.J. Eksteen, and S.M. Bradshaw: *Miner. Eng.*, 2013, vol. 46, pp. 16–24.
42. G.J. Chen, S.P. He, and Y.G. Li: *Metall. Trans. B*, 2017, vol. 48B, pp. 2176–86.
43. L.M. Li and B.K. Li: *JOM*, 2016, vol. 68, pp. 2160–69.
44. Y. Li, W.T. Lou, and M.Y. Zhu: *Ironmak. Steelmak.*, 2013, vol. 40, pp. 505–14.
45. M. Sano, K. Mori, and Y. Fujita: *Tetsu-to-Hagane*, 1979, vol. 65, pp. 1140–48.
46. Q. Cao and L. Nastac: *JOM*, 2018, vol. 70, pp. 2071–81.
47. H. Ling and L. Zhang: *Metall. Trans. B*, 2018, vol. 49B, pp. 2709–21.
48. W.X. Dai, G.G. Cheng, S.J. Li, Y. Huang, and G.L. Zhang: *ISIJ Int.*, 2019, vol. 59 (12), pp. 2228–38.
49. L. Zhang and F. Li: *JOM*, 2014, vol. 66, pp. 1227–40.
50. V. Seshadri and S.L.S. Costa: *Trans. Iron Steel Inst. Jpn.*, 1986, vol. 26, pp. 133–38.
51. L. Neves, H. Oliveira, and R.P. Tavares: *ISIJ Int.*, 2009, vol. 49 (8), pp. 1141–49.
52. L. Zhang and C. Liu: *Ironmak. Steelmak.*, 2018, vol. 45, pp. 145–56.
53. H. Lei and J. He: *Ironmak. Steelmak.*, 2012, vol. 39, pp. 431–38.

Publisher's Note Springer Nature remains neutral with regard to jurisdictional claims in published maps and institutional affiliations.